

See discussions, stats, and author profiles for this publication at: <https://www.researchgate.net/publication/47716821>

# Decoupling Electrochemical Reaction and Diffusion Processes in Ionically-Conductive Solids on the Nanometer Scale

ARTICLE in ACS NANO · NOVEMBER 2010

Impact Factor: 12.88 · DOI: 10.1021/nn101502x · Source: PubMed

CITATIONS

46

READS

90

7 AUTHORS, INCLUDING:



Nina Balke

Oak Ridge National Laboratory

98 PUBLICATIONS 2,843 CITATIONS

SEE PROFILE



Yoongu Kim

SolidEnergy Systems, Boston, USA

16 PUBLICATIONS 322 CITATIONS

SEE PROFILE



Nancy J Dudney

Oak Ridge National Laboratory

191 PUBLICATIONS 5,351 CITATIONS

SEE PROFILE



Sergei V Kalinin

Oak Ridge National Laboratory

623 PUBLICATIONS 11,091 CITATIONS

SEE PROFILE

# Decoupling Electrochemical Reaction and Diffusion Processes in Ionically-Conductive Solids on the Nanometer Scale

Nina Balke,<sup>†</sup> Stephen Jesse,<sup>†</sup> Yoongu Kim,<sup>‡</sup> Leslie Adamczyk,<sup>‡</sup> Ilia N. Ivanov,<sup>†</sup> Nancy J. Dudney,<sup>‡</sup> and Sergei V. Kalinin<sup>†,\*</sup>

<sup>†</sup>Center for Nanophase Materials Sciences and <sup>‡</sup>Materials Science and Technology Division, Oak Ridge National Laboratory, Oak Ridge, Tennessee 37831, United States

Solid-state electrochemical processes underpin a broad spectrum of energy and information storage devices, ranging from Li-ion<sup>1</sup> and Li-air batteries,<sup>2</sup> to solid oxide fuel cells (SOFC)<sup>3</sup> to electroresistive<sup>4</sup> and memristive<sup>5</sup> systems. These functionalities are controlled by the bias-driven diffusive and electromigration transport of mobile ionic species,<sup>6–8</sup> as well as an intricate set of electrochemical and defect-controlled reactions at interfaces<sup>9–12</sup> and in bulk.<sup>13</sup> Multiple examples include generation, transport, and ordering of oxygen vacancies in memristive systems and SOFC materials<sup>14,15</sup> or coupled electronic and ionic transport phenomena in batteries.<sup>1</sup> Understanding and optimization of these materials and devices have necessitated the development of a broad spectrum of electrochemical characterization tools ranging from conductivity measurements to intricate time- and frequency spectroscopies.<sup>16,17</sup> To date, the vast majority of these methods are based on the detection of electronic (either electrochemical Faradaic, capacitive, or conductive) currents in time and frequency domains.

The current tendency toward the miniaturization of energy storage and information technology devices as well as the need for better understanding of the fundamental mechanisms of coupling between structure and electrochemical functionality necessitates that ionic transport and interfacial reactivity be probed on the nanoscale level of a single nanoparticle, grain edge, or individual structural defect. However, the existing solid-state electrochemical methods invariably utilize slow and large scale ion-conducting electrodes,<sup>18,19</sup> limiting these

**ABSTRACT** We have developed a scanning probe microscopy approach to explore voltage-controlled ion dynamics in ionically conductive solids and decouple transport and local electrochemical reactivity on the nanometer scale. Electrochemical strain microscopy allows detection of bias-induced ionic motion through the dynamic (0.1–1 MHz) local strain. Spectroscopic modes based on low-frequency (~1 Hz) voltage sweeps allow local ion dynamics to be probed locally. The bias dependence of the hysteretic strain response accessed through first-order reversal curve (FORC) measurements demonstrates that the process is activated at a certain critical voltage and is linear above this voltage everywhere on the surface. This suggests that FORC spectroscopic ESM data separates local electrochemical reaction and transport processes. The relevant parameters such as critical voltage and effective mobility can be extracted for each location and correlated with the microstructure. The evolution of these behaviors with the charging of the amorphous Si anode in a thin-film Li-ion battery is explored. A broad applicability of this method to other ionically conductive systems is predicted.

**KEYWORDS:** scanning probe microscopy · Li-ion batteries · solid state ionics

studies to the ~10  $\mu\text{m}$  scale. This scale is well above the characteristic size of grains in electrode composites, extended defects such as dislocations or antiphase boundaries, or active zones of nanoscale electroresistive, memristive, and phase-change devices. At the same time, classical (electronic) current- and force-based scanning probe microscopy (SPM) techniques have only limited applicability for probing mass currents in solids, such as cation and oxygen vacancy diffusion.<sup>20</sup>

Recently, we have developed a scanning probe microscopy-based approach, referred to as electrochemical strain microscopy (ESM), for detecting and mapping Li-ion currents in solids on the nanoscale.<sup>21–23</sup> In ESM, a high frequency periodic bias is applied between the tip and an electrochemically active material surface (tip-electrode) or between top and bottom electrodes of an active electrochemical device (top-electrode). The SPM tip acts as a probe of

\*Address correspondence to sergei2@ornl.gov.

Received for review July 2, 2010 and accepted October 29, 2010.

Published online November 8, 2010. 10.1021/nn101502x

© 2010 American Chemical Society

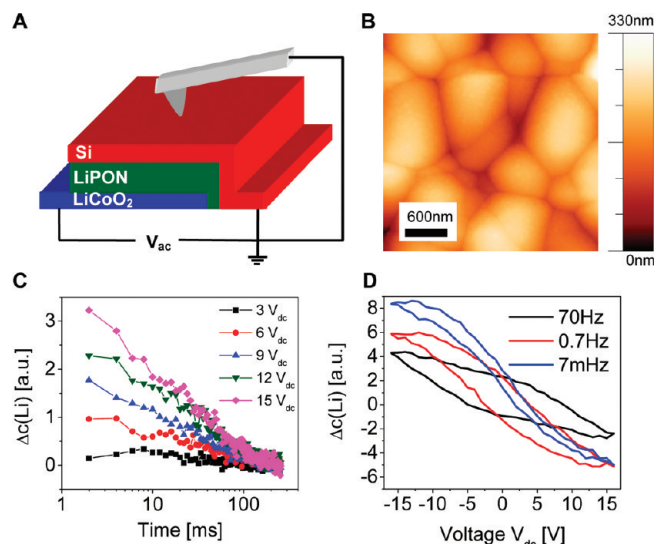


**Figure 1.** (a) Schematics of the battery structure; (b) surface topography of Si anode; (c) ESM relaxation signal after voltage pulses of increasing amplitude; (d) hysteretic response for voltage spectroscopy ESM.

local periodic strains generated because of bias-induced Li-ion redistribution and associated changes in molar volume of the material. The intrinsically high sensitivity of AFM to small ( $\sim 2\text{--}5$  pm level) oscillatory surface displacements combined with high ( $10\text{--}20$  nm) lateral resolution allows Li-ion motion to be probed in  $\sim 10^6$  smaller volumes than possible by classical current-based electrochemical methods.<sup>24</sup> Previously, we have demonstrated the use of ESM for the spatially resolved mapping of Li-ion dynamics in Si-anode materials.<sup>22</sup> Here, we demonstrate that spectroscopic 2D first-order reversal curve (FORC) measurements in ESM allow voltage activated Li-ion flows to be measured *locally*, demonstrating that the process is activated at a certain critical voltage and is linear above it. This observation suggests that the local electrochemical reaction and transport processes can now be decoupled and probed independently on the single defect level.

## RESULTS AND DISCUSSION

**Bias-Dependent Mapping of Li-Ion Flow.** As a model system, we have chosen an all-solid thin-film Li-ion battery test structure<sup>25</sup> with the bottom LiCoO<sub>2</sub> cathode, nitrogen-doped lithium phosphate (LiPON) electrolyte, and top Si anode, as shown schematically in Figure 1a. Similarly to piezoresponse force microscopy of ferroelectric capacitors,<sup>26–28</sup> the use of the device-biasing scheme with the bottom electrode biased suggests that the electromechanical response detected by the tip is generated primarily as a material response to a macroscopically uniform electric field within the battery device and is unrelated to electrostatic tip–surface forces. For a conductive anode, the equality of tip and top electrode potentials will ensure the absence of tip–surface currents and hence electrochemical processes in the tip–surface junction. The presence of a protective SiO<sub>2</sub>

layer further suppresses any direct tip–surface reactivity. For semiconducting materials with limited conductivity, the potential on the anode surface can differ from that of the current collector (sharing common ground with the tip), thus potentially leading to a potential drop in the tip–surface junction. In this case, the ESM contrast can originate due to ionic flow in the tip–surface junction, while the electrode structure enables systematic control of the average Li-ion concentration in the anode.

Figure 1b shows the topography of the Si anode measured with the AFM tip. The anode shows clear grain boundary-like features (despite the amorphous nature of the Si) that form due to the substrate roughness. The observed topography of the amorphous Si layer is very similar to what has been reported in literature. It was shown that cross sections of thin film amorphous Si structures show 30–50 nm columnar features.<sup>29–31</sup>

Application of a bias to the battery structure induces the redistribution of Li-ions by migration and diffusion mechanisms driven by the changes in the electrostatic potential and concentration gradients, respectively. We will refer to the bias-induced Li redistribution as Li-ion flow throughout the paper, leaving the elucidation of exact transport mechanisms (diffusion vs migration) to future studies. Owing to the strong coupling of Li concentration and sample volume, the change in Li concentration,  $c(\text{Li})$ , results in local strains and hence in a surface displacement that can be locally detected with the SPM tip. To probe the Li concentration without changing the charging state of the battery, high-frequency ( $\sim 400$  kHz) AC bias with 2 V<sub>ac</sub> amplitude are applied. The use of high frequencies well above inverse diffusion times (*ca.* for  $\sim 10$  nm diffusion length) of material results in only small changes in  $c(\text{Li})$  in response to bias oscillations. At the same time, periodic excitation allows using the lock-in technique to detect pm-range surface displacement. Here, we further use the band excitation (BE) method<sup>32</sup> to effectively track surface resonances of the cantilever. The amplitude of surface oscillations at the cantilever resonance comprises the ESM signal and is a measure for the concentration change  $\delta c(\text{Li})$  induced by the AC bias. The simultaneously measured resonant frequency and quality factor are a measure of the elastic properties of the surface and surface topography and are not studied further (note that the resonance frequencies can change by as much as 50 kHz across the surface, as compared to *ca.* 3–5 kHz resonance peak width, thus necessitating the use of BE or similar non phase locked loop based methods<sup>33–36</sup>). The measured ESM signal scales linearly with V<sub>ac</sub> in the 1–6 V<sub>ac</sub> range at 400 kHz, suggesting a linear relationship between the driving force (the applied voltage) and the Li concentration. The quantification of the ESM signal requires the complete analysis of the drift-diffusion ion dynamic in the presence of a

bias, and is the subject of further studies. However, the relative changes of the ESM signal across the interface can be interpreted as changes in the Li-ion concentration and mobility.

The ESM signal can be used to investigate Li-ion migration and diffusion in biased and unbiased structures. For that, high voltage pulses,  $V_{dc}$ , are applied between the top and bottom electrodes for short times. Typical pulse amplitudes and times are 3–15  $V_{dc}$  and 2 ms to 1 s, respectively. The short pulse lengths allow applying high voltages without detectable damage, since Li-ion transport and stray reaction kinetics are significantly slower ( $\sim 10$ s of minutes) than pulse length. The voltage pulse induces a change of Li-ion concentration through electromigration and diffusion mechanisms. When the DC bias is turned off, the redistribution of Li-ion through diffusion takes place. These processes on the millisecond to ten second scales can be tracked using ESM as the high-frequency electromechanical response of the surface (*i.e.*, ESM amplitude). The ESM signal as a function of time after application of several voltage pulses with amplitudes from 3 to 15  $V_{dc}$  with a pulse length of 1 s are shown in Figure 1c.

The pulses with the higher amplitude result in larger changes in Li-ion concentration over larger distances. Correspondingly, the introduced concentration gradients, and thus the changes in the ESM signal, are higher. Note that the relaxation time is comparable for all pulse magnitudes/lengths, and thus is only a weak function of total Li concentration.

To map the Li-ion flow in the anode material, we perform spatially resolved voltage spectroscopy ESM. In this mode, short voltage pulses ( $\sim 2$  ms) of increasing and decreasing amplitude are applied between the cathode and anode and the ESM signal is measured directly after each pulse (corresponds to the first measurement point in Figure 1c). Typical  $V_{dc}$  sweep rates are *ca.* 1–10 Hz. In this manner, the redistribution of Li-ions on the time scale of the waveform (*ca.* 0.1–1 s) is probed through the changes of high-frequency ( $\sim 300$  kHz) electromechanical activity. The result of the voltage spectroscopy is shown in Figure 1d. The ESM amplitude response induced by the  $V_{dc}$  pulses shows a clear hysteretic behavior. The origins of the observed hysteretic response can be simply understood from the consideration of frequency-dependent Li-ion dynamics on the length scale of the detection volume of an SPM probe. For very high frequencies the Li ions are barely moving, hence the response is small and the hysteresis loop is closed. This is the frequency regime used to probe the strain response with the BE waveform (using  $V_{ac}$ ) that results only in minute changes of Li-ion distribution through diffusion<sup>23</sup> and electromigration mechanisms. With decreasing frequency the amplitude increases and the hysteresis loop opens, since Li redistribution on the length scale of probing volume is possible (note that low frequency  $\sim 1$  Hz waveform re-

sults in periodic Li-ion redistribution, and the high frequency BE waveforms takes the “snapshots” of Li concentration), but the concentration field changes with the probing volume lag behind the field. Finally, for very low frequencies the Li redistribution occurs on the length scales well above the signal generation volume of an SPM probe or local defects. In this regime, the response saturates and the hysteresis loop closes and becomes S-shaped. Shown in Figure 1d are dynamic strain loops for three different DC sweep frequencies, illustrating evolution from a low-frequency S-shape to an unsaturated high-frequency shape, which agrees well with theoretical expectations.<sup>22</sup>

**Bias-Dependence of Hysteretic Responses.** The characteristic aspect of the hysteretic behavior is that the loop parameters and shape can strongly depend on the field history. The theory of field-dependent hysteresis is well-developed for systems having a distribution of thermodynamic switching parameters, for example, Preisach-type models.<sup>37</sup> For electrochemically active systems, the initiation of diffusive transport may require the driving voltage to exceed a certain threshold value corresponding to the generation of diffusing species. While this behavior cannot be captured by a single measurement, systematic studies of system responses for different field histories can often reveal underlying mechanisms.<sup>38</sup>

Here, we explore the local bias-dependent Li-ion dynamics using voltage spectroscopy ESM. A sweep frequency of 7 Hz was used and loops with increasing envelope voltage  $V_f$  (*i.e.*, maximum pulse amplitude  $V_{dc}$  during voltage sweep) were measured on a  $70 \times 70$  point grid in a  $1 \times 1 \mu\text{m}^2$  area (14 nm pixel size) chosen to include a boundary-like topography feature. The loop opening was analyzed as a measure of the amount of Li-ion redistributed through the voltage sweep. Shown in Figure 2 is the hysteresis loop opening maps as a function of bias window. Note that the relative intensity of the features exhibits strong bias dependence; for example, for a small bias window the contrast on the grain boundaries is clearly seen, while the “hot spots” within the grain are relatively weak. At the same time, for higher bias windows the intensity of the grain boundary feature as well as the hot spots becomes significantly higher. While the exact nature of the hot spots is not clear, they likely correspond to defects underneath or within the anode.

The data in Figure 2 suggests that the hysteretic ESM response is activated only above a certain voltage threshold, and increases monotonically (but with position-dependent behavior) above it. This behavior suggests a possible interpretation that the threshold voltage indicates a transition from a reaction-limited to a transport-controlled process. Indeed, for a typical electrochemical reaction–diffusion system, the reaction rate is related to overpotential as



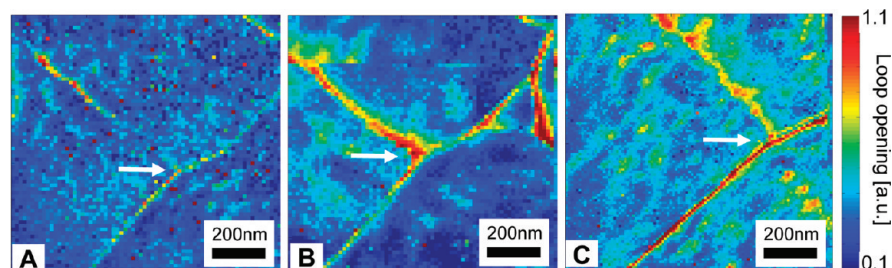


**Figure 2.** Bias dependence of the hysteresis loop opening maps. Shown are the maps at (A) 10, (B) 12, and (C) 15 V bias windows. Note that because of the sequential image acquisition, the images are shifted with respect to each other due to microscope drift. The arrow indicates the three grain-boundary junction that serves as a common reference point.

$$v = k \exp \left[ \alpha \frac{V - V_0}{V} \right] \quad (1)$$

The reaction does not proceed for biases below the corresponding redox potential (*i.e.*, negative overpotential). The reaction rate increases almost exponentially (Tafel-like dependence) above the critical potential  $V_0$ . In the systems including mass-transport stage, the overall kinetics becomes transport-limited typically for  $(V - V_0) > 0.2$  V.<sup>16</sup> Note that here transport refers to both electromigration (*i.e.*, flow linear in electric field) and diffusion (flow linear in concentration gradient) mechanisms.

Two specific aspects of this behavior must be specifically mentioned. First, the rapid (in the bias interval of 0.1–0.2 V) transition from the reaction-limited to the transport-limited process suggests that measuring the response as a function of varying the maximum pulse amplitude  $V_f$  in ESM hysteresis loop measurements may allow reaction onset and Li-ion flow to be separated, as schematically illustrated in Figure 3. Second, we note that the Li-ion flow is linear in the driving force, and hence in this regime the ESM signal should depend linearly on the excitation bias  $V_f$  in the form of  $\Delta c(\text{Li}, 0 V_{dc}) = a + bV_f$ . The slope  $a$  of the linear fit is directly correlated to the Li-ion flow under bias, whereas the intercept with the x-axis  $V_{fc} = -a/b$  is the critical voltage needed for the activation of reaction process.

In the subsequent sections, we (a) develop the approach for the spatially resolved mapping of multiple hysteresis loops at each point over spatial grid, (b) de-

velop the multivariate analysis of the response signal that allows the linear signal to be determined, and (c) use these approaches to identify and separate reaction and transport stages of bias-induced Li-ion flow.

**First-Order Reversal Curves Measurements.** To deconvolute the transport and electrochemical reactivity, we introduce first-order reversal curve measurements in ESM voltage spectroscopy. In this mode, the measurements at each location were performed as a function of bias sweep amplitude (excitation window) at each location, using the waveform shown in Figure 4c. Here, we refer to this mode as W first-order reversal curves (W-FORC). In this case, the set of hysteresis loops are obtained as a function of excitation window at each spatial location with perfect spatial correlation, obviating the need for spatial alignment of maps obtained sequentially. Previously, these SPM-based FORC measurements have been implemented for ferroelectric materials in the single-point<sup>39</sup> modes and spatially resolved measurements in the tip-electrode<sup>40</sup> and top-electrode, that is, capacitor structures, geometries. The manuscripts (refs 39 and 40) describe the technical aspects of acquisition, visualization, and analysis of high-dimensional data (5D for the full FORC-BE-SSPFM data sets, with *ca.* 30–40 GB data files).

The envelope of the excitation waveform and the 2D spectrogram of the amplitude and phase response as a function of frequency and time are shown in Figure 4 A,B. The changes in response amplitude and phase jumps by 180° are clearly seen, similar to the behavior observed during polarization switching in ferroelectric materials. At the same time, the resonance frequencies (corresponding to maxima of the response) depend on bias only weakly (variation is less than ~1 kHz, as compared to ~20 kHz between dissimilar locations, and ~3 kHz peak width), consistent with the high stability of the tip surface contact for oxidized Si surface. The strain response loops,  $PR(V_{dc}) = A \cos(\varphi)$ , can be extracted by integrating the resonance amplitude peak and are shown in Figure 4D. The resulting response–voltage hysteretic response provides an electromechanical analog of the cyclic voltammogram. Note the hysteresis loop at a single selected location is closed for  $V_f < 4$  V, indicating that no Li-ions are moving under the applied field at a frequency of 7 Hz. As the

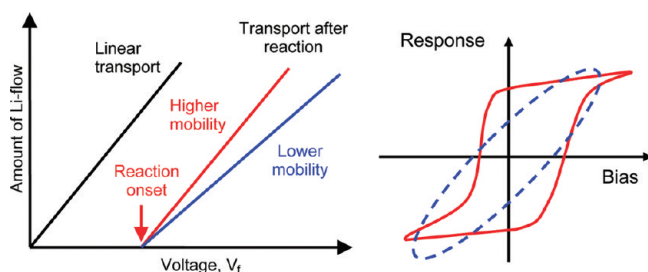


**Figure 3.** (a) The schematic illustration of the Li-redistribution as a function of maximum bias pulse  $V_f$ . In the presence of the reaction limitation, the process is linear above certain threshold bias. (b) The expected change of the hysteretic response. The reaction step provides the inflection point (“nucleation bias”) compared to the elliptic transport-limited loops.

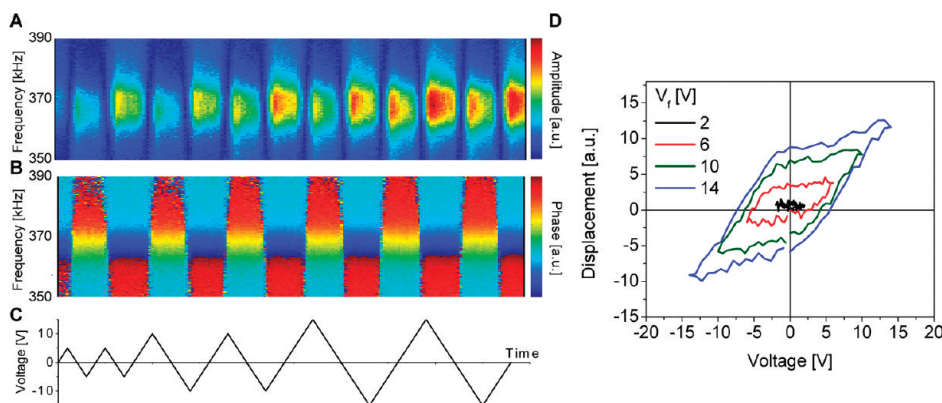


**Figure 4.** Amplitude and phase for six subsequent bias sweeps with increasing envelope voltage (signal is averaged over 20 points on a grain boundary). Examples for extracted displacement loop as a function of envelope voltage.

maximum bias voltage increases, the strain response loop is opening up linearly with increasing  $V_i$ .

The advantage of this approach is illustrated in Figure 5, in which the hysteresis loop opening maps (*i.e.*, remanent hysteretic ESM response) are plotted as a function of the bias window. The evolution of the contrast on the grain boundary feature and a selected hot spot is clearly seen and can now be compared on a pixel-by-pixel basis. Note that each spatial location contains the full FORC BE data set similar to that shown in Figure 4.

**Multivariate Statistical Analysis and Signal Assignment.** The systematic analysis of the bias-dependence of the ESM signal requires quantitative understanding of the signal formation mechanisms to parametrize bias-dependent Li flow (*i.e.*, electrochemical activity) and relate it to a properly chosen experimental signal (*e.g.*, area under the loop, remanent response, saturated response, or other characteristic loop features).<sup>41</sup> Ideally, such interpretation is possible once a proper physical model (*e.g.*, Hertzian contact for contact mechanics) is known. However, the complexity of response mechanism in ESM (as is the case for many other SPM modes) precludes such model-based data analysis in this case. As an alternative, multivariate statistical analysis methods can be used to establish the pathway for data analysis, once the proper hypothesis is available. Here, we assume that transport-related (*i.e.*, diffusion or electromigration) response is linear in driving force above the certain critical bias, as described above, and search for the appropriate form of the ESM signal that best satisfies this condition at each location on the sample surface (*i.e.*, for eight FORC loops at each of the  $10^4$  locations of a  $100 \times 100$  pixel image).

To perform this analysis systematically, we employ principal component analysis<sup>42–44</sup> of the 3D  $SP(x, y, V_i)$  data arrays, where  $SP$  is the characteristic hysteresis loop parameter (*e.g.*, loop opening),  $(x, y)$  is coordinate, and  $V_i$  is the bias window. The spectroscopic image of  $N \times M$  (here,  $N, M = 100$ ) pixels formed by spectra containing  $P$  points (here,  $P = 8$ ) is represented as a superposition of the eigenvectors  $w_j$ ,

$$SP_i(V_j) = a_{ik}w_k(V_j) \quad (2)$$

where  $a_{ik} \equiv a_k(x, y)$  are position-dependent expansion coefficients,  $SP_i(V_j) \equiv SP(x, y, V_i(j))$  is the hysteresis loop opening image at a selected excitation window, and  $V_j = V_i(j)$  are the excitation windows for which hysteresis loop openings are measured. The summation on the repetitive indices in eq 2 is implied. The eigenvectors  $w_k(V_j)$  and the corresponding eigenvalues  $\lambda_k$  are found from the covariance matrix,  $C = AA^T$ , where  $A$  is the matrix of all experimental data points  $A_{ji} = SP_i(V_j)$ , that is, the rows of  $A$  correspond to individual grid points ( $i = 1, \dots, N \cdot M$ ), and columns correspond to voltage points,  $j = 1, \dots, P$ . The eigenvectors  $w_k(V_j)$  are orthogonal and are chosen such that corresponding eigenvalues are placed in descending order,  $\lambda_1 > \lambda_2 > \dots$ . The eigenvalues and eigenvectors are determined through singular value decomposition of the  $A$  matrix.

The principal component analysis (PCA) was performed on a selected region of the sample surface. For  $SP$  = hysteresis loop opening, the spatial maps of the first three PCA components and corresponding eigenvectors and eigenvalues are shown in Figure 6. The shape of  $\lambda_k(k)$  dependence (scree plot) indicates that the first  $p = 3$  PCA components contain 83% of the significant information within the 3D spectral image. This behavior is also evident from the spatially resolved maps of the first, second, and third PCA loading components that clearly illustrate long-range contrast and discernible spatial features, whereas the fourth and subsequent PCA maps are essentially random noise (note that

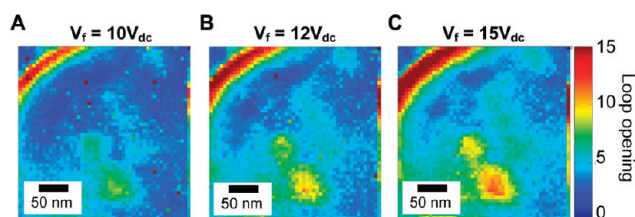


**Figure 5.** Bias dependence of the hysteresis loop opening maps extracted from loop opening maps. Unlike the data in Figure 2, the responses at different voltages are perfectly correlated spatially, allowing for systematic studies of the bias-dependent response for each location.



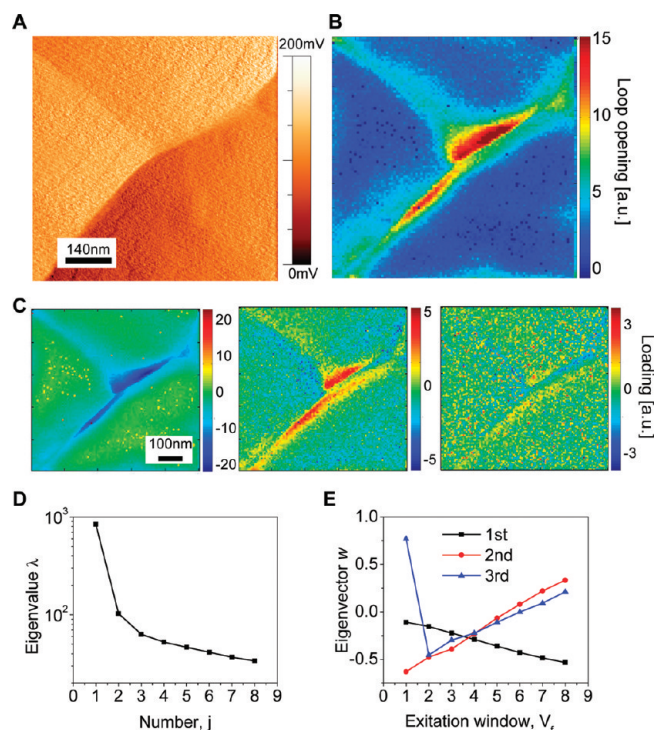


**Figure 6.** Principal component analysis of the FORC data. (A–C) Loading maps corresponding to first three PCA components (the 4th and higher maps are essentially noise-driven). (D) The scree plot and (E) the first three eigenvectors.

classical PCA selection criteria,<sup>45</sup> based on the shape of the scree plot only, clearly suggest that the first two components are important and that the third is potentially important). Notice that clearly visible features are predominantly concentrated in the first and second PCA loading maps. This strongly suggests that the variability of the hysteresis loop-opening behavior (*i.e.*, Li-

ion dynamics) can be adequately described by only two independent variables.

The first three eigenvectors,  $w_k(V_j)$ , are shown in Figure 6E. Note that the first two components are almost linear, with the first being given by  $w_1(V_j) = (-0.78 \pm 0.02) + (0.140 \pm 0.003)V_j$ , that is, almost direct proportionality, and the second  $w_2(V_j) = (-0.038 \pm 0.007) - (0.063 \pm 0.001)V_j$ , that is, strong offset component. The third eigenvector contains the linear dependence (almost similar to the second component) as well, with the outlier in the first voltage point. Hence, this analysis suggests that on average the individual spectra within the 3D spectroscopic relaxation image are best represented as the linear response above a critical bias,  $SP_i(V_j) = a + bV_j$ , as is used throughout the paper.

Furthermore, this analysis illustrates that loop opening is indeed the parameter that best describes Li ion transport, since for all other hysteresis loop descriptions the PCA eigenvectors are not linear functions of voltage. Finally, note that PCA analysis is purely statistical and does not employ any assumption regarding underlying physical behavior, ensuring its fidelity.

**Decoupling of Reaction and Diffusion Process.** The linear form of response allows the decoupling of the critical voltage for reaction onset,  $V_o$ , and the Li-ion transport linear in field (referred to as effective mobility), as shown schematically in Figure 3A. To achieve this, the hysteretic response vs voltage data at each spatial point is fitted by the linear function,  $y = ax + b$ . The fitted slope  $a$  and intercept  $b$  are shown in Figure 7 panels A and B, respectively, demonstrating a clear linear trend with the critical bias  $V_{fc}$  generally varying between 0 and 5 V. Note that this value is close to the potential of a Si–LiCoO<sub>2</sub> battery. The calculated critical bias map  $V_{fc} = -b/a$  is shown in Figure 7C. The regions with slopes close to zero (regions between the boundaries) result in a large scatter of the fitted value for  $V_{fc}$  which is visible in the map in Figure 7C as negative values for the critical bias. Figure 7D points out different loop opening vs voltage curves including the linear fit for four characteristic regions which are denoted in Figure 7C. The regions a and b (black and red) within the highly active boundary have different slopes, but an almost similar reaction onset voltage of  $\sim 5$  V. Region c (blue) is along the less active boundary showing a linear diffusion curve, meaning the intercept value is zero. Region d (green) shows the lowest slope, indicative of low effective mobility of Li-ions.

#### Evolution of ESM Response during High Frequency Cycling.

The long-term observations of the ESM response during cycling have illustrated the presence of slow dynamic changes, as described in the manuscript. Shown in Figure 8A–D is the evolution of the critical bias and mobility (slope of linear fit) as a function of the number of cycles (up to  $6 \times 10^5$  sinusoidal cycles of 16 V amplitude at 7 Hz rate). The ESM maps (not shown here),

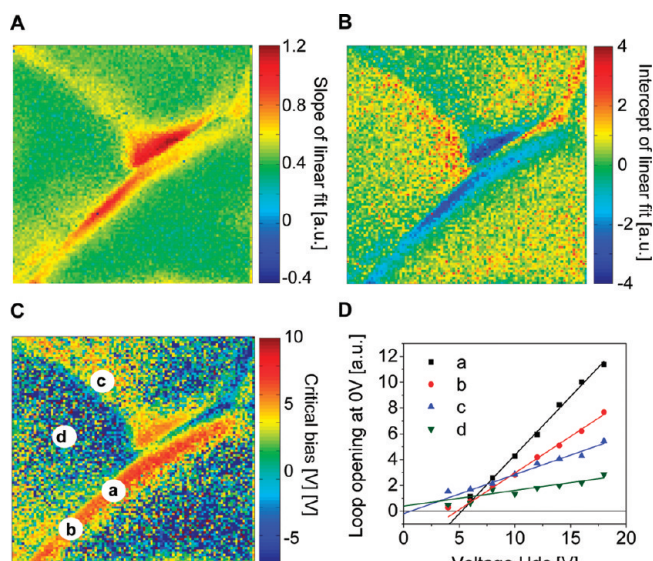


**Figure 7.** Separation of reaction and transport phenomena. (A) Loop opening map of strongly cycled battery (same region as shown in Figure 4A). (B) Slope  $a$  and (C) critical bias (*i.e.*,  $x$ -axis intercept from linear fit of loop opening) as a function of maximum dc voltage  $V_f$ . (D) Example curves with fit from four different points in different regions from panel C.

show the gradual evolution of contrast at “hot spots” and grain boundaries. While in the beginning of the process both defect types are involved in Li dynamics equally, after cycling only strong ESM activity at grain boundaries is visible.

The maps shown in Figure 8 were extracted from a FORC-type measurement that contains loop opening as a function of voltage. Correspondingly, the evolution of reaction onset bias and effective mobility with cycling can be explored. The evolution of the critical reaction onset voltage  $V_{fc}$  after different cycle numbers are shown in Figure 8A. While in the pristine state the critical reaction onset is almost position independent and centered around zero, in the cycled state it achieves the value of  $\sim 4$  V in the grain-boundary regions. The corresponding histograms are shown in Figure 8 panels C and D. The histogram of slopes illustrates the formation of regions with enhanced effective mobility as well.

Hence, the high frequency cycling changes the Li-ion behavior along the boundaries which is now a voltage activated process. This is directly related to the changes in electrochemical behavior of the battery upon Li intercalation and suggests a highly nonuniform distribution of Li activity within the anode material.

## SUMMARY

We demonstrate that Li-ion flow mediated coupling between bias and strain allows mapping of local mobility and electrochemical reactivity in Si anode material in battery devices. The use of the SPM tip to detect local strain on the oxide-passivated surface allows highly reproducible measurements in an ambient environment without visible changes in surface structure even after multiple measurement cycles. The use of complex band-excitation waveforms allows the frequency regimes of Li-ion response to be decoupled, optimizes response–resolution relation, and effectively utilizes cantilever resonances to achieve high-signal/noise ratios and eliminate topographic cross-talk. While the exact contrast formation mechanism (tip-controlled or top electrode controlled) is still an open question, the comparative measurements of response across the surface provide insight into the local electrochemical functionality and its evolution during the charging process.

The measurements of the Si anode material illustrate effective spatial resolutions below 10 nm, comparable with defect spacing and well below characteristic grain sizes. The ESM maps clearly illustrate the presence of active transport pathways at sharp grain boundaries and the presence of multiple hot-spots associated with (as yet unidentified) defects. The measurement of strain response amplitude at each location as a function of excitation window allows the local effective mobility and the critical potential for the onset of electrochemical re-

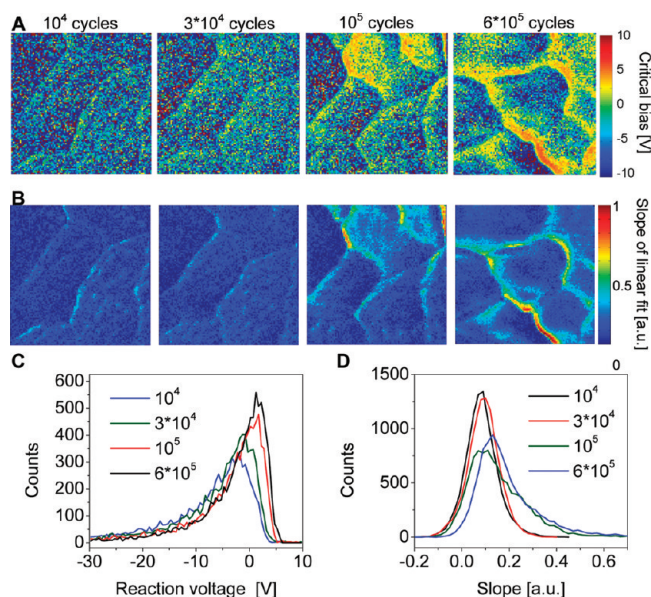


**Figure 8.** Evolution of (A) critical bias and (B) effective mobility during cycling. Shown are maps measured with 16 V bias window (outer loop of the W-FORC series) after  $10^4$ ,  $3 \times 10^4$ ,  $10^5$ , and  $6 \times 10^5$  sinusoidal cycles at 7 Hz, respectively. Histograms of (C) critical bias and (D) effective mobility extracted from W-FORC measurements. The negative tails originate from the regions with zero response.

action to be decoupled and correlated with morphological features. Finally, the evolution of the voltage-dependent Li-ion flow behavior during the bias-induced battery changes was mapped, and the response was shown to be evolving from the nearly uniform to the highly localized at the grain boundary sites.

These studies hence provide previously unavailable insight into the internal functionality of Li-ion batteries, providing high-veracity, real space mapping of transport, and electrochemical reactivity. The frequency-, time-, and voltage spectroscopic modes of the ESM suggest the potential for performing traditional electrochemical measurements in nanoscale volumes of material. While the current studies were enabled by the intrinsic passive layer on Si surface, measurements in controlled atmosphere will allow extending this approach to other energy materials, all of which possess high  $c(\text{Li})$ –strain coupling. Furthermore, given that the chemical expansivity, that is, changes in material volume as a function of the concentration of a mobile component (metal cation, oxygen vacancies) is a ubiquitous feature of all ionic and mixed ionic-electronic conductors and has been demonstrated for ceria,<sup>46</sup> cobaltites,<sup>47–50</sup> nickelates,<sup>51</sup> and manganites,<sup>52</sup> the ESM imaging and spectroscopy can be expected to be broadly applicable for these materials as well. Recent electron microscopy studies suggest that this response can be detected locally down to the 1 nm level.<sup>53</sup> A comparison with ferroelectric materials<sup>54–56</sup> suggests that these studies can be performed at the level of single structural defects. Furthermore, the use of media with controlled H and O activity will allow this



approach to be established for mapping  $H^+$  and  $O^{2-}$  diffusivity in proton conductors and fuel-cell materials,

as well as intricate phenomena underpinning memristive materials and devices.

## MATERIALS AND METHODS

The rechargeable thin-film batteries obtained here consisted of Si/Lipon/LiCoO<sub>2</sub> structures on Au/Ni-coated Al<sub>2</sub>O<sub>3</sub> substrates. Before depositing the LiCoO<sub>2</sub> cathode films, an Al stencil mask was used to cover the Au/Ni-coated Al<sub>2</sub>O<sub>3</sub> substrates and define the cathode areas with 0.2 cm diameter. The  $\sim 0.5$   $\mu$ m thick LiCoO<sub>2</sub> cathode films were fabricated on the substrates using a RF-magnetron sputtering technique at 50 W deposition power (159 V). The films were annealed at 800 °C for 2 h in an O<sub>2</sub> flowing quartz tube furnace. The amorphous LiPON electrolytes ( $\sim 1$   $\mu$ m thick) were deposited on the LiCoO<sub>2</sub> films using the same sputtering technique with 70 W (230 V). Finally, amorphous Si anodes of  $\sim 350$  nm thickness were deposited on the LiPON film electrolytes using a DC-magnetron sputtering technique.

**Methods.** Atomic force microscopy (AFM) measurements were performed on a commercial system (Veeco Dimension) equipped with LabView/MatLab-based band excitation controller implemented on a PXI-5122/PXI-5412 fast DAQ card. Imaging was performed with 200–400 kHz 2 V<sub>ac</sub> band excitation signal applied to the bottom electrode of the battery device. This bias amplitude is chosen well within the linearity regime of the response. The AFM tip (Nanosensors, Pt/Ir coating) and the top electrode were grounded to minimize electrostatic signal contribution and electrochemical processes at tip–surface junction. The spectroscopic measurements were performed at  $\sim 1$  s/pixel waveform with 2 ms at each step. The typical acquisition time of the 5D FORC BE SSPFM data set formed by  $100 \times 100$  pixel with 150 frequency points and 13 voltage points (corresponding to 26 hysteresis loops) is 40 h. The typical file size is  $\sim 3$  GB for BEPS mode and  $\sim 30$  Gb for FORC BEPS mode.

**Acknowledgment.** This material is based upon work supported as part of the Fluid Interface Reactions, Structures and Transport (FIRST) Center, an Energy Frontier Research Center funded by the U.S. Department of Energy, Office of Science, Office of Basic Energy Sciences under Award Number ERKCC61 (N.D.). Research at the ORNL's Center for Nanophase Materials Sciences (SVK) in the project CNMS2010-098 and CNMS2010-099 was sponsored by the Scientific User Facilities Division, Office of Basic Energy Sciences, U.S. Department of Energy (N.B., S.J., I.N.I.). N.B. acknowledges the Alexander von Humboldt foundation for financial support.

## REFERENCES AND NOTES

- Nazri, G. A.; Pistoia, G. *Lithium Batteries: Science and Technology*; Springer-Verlag: New York, 2009.
- Abraham, K. M.; Jiang, Z. A Polymer Electrolyte-Based Rechargeable Lithium/Oxygen Battery. *J. Electrochem. Soc.* **1996**, *143*, 1–5.
- O'Hayre, R.; Cha, S. W.; Colella, W.; Prinz, F. B. *Fuel Cell Fundamentals*; John Wiley & Sons: New York, 2009.
- Sawa, A. Resistive Switching in Transition Metal Oxides. *Mater. Today* **2008**, *11*, 28–36.
- Strukov, D. B.; Snider, G. S.; Stewart, D. R.; Williams, R. S. The Missing Memristor Found. *Nature* **2008**, *453*, 80–83.
- Li, S. L.; Gang, J. L.; Li, J.; Chu, H. F.; Zheng, D. N. Reproducible Low-Voltage Resistive Switching in a Low-Initial-Resistance Pr<sub>0.7</sub>Ca<sub>0.3</sub>MnO<sub>3</sub> Junction. *J. Phys. D* **2008**, *41*, 185409.
- Fujii, T.; Kawasaki, M.; Sawa, A.; Kawazoe, Y.; Akoh, H.; Tokura, Y. Electrical Properties and Colossal Electroresistance of Heteroepitaxial SrRuO<sub>3</sub>/SrTi<sub>1-x</sub>Nb<sub>x</sub>O<sub>3</sub> ( $0.0002 \leq x \leq 0.02$ ) Schottky Junctions. *Phys. Rev. B* **2007**, *75*, 165101.
- Borghetti, J.; Strukov, D. B.; Pickett, M. D.; Yang, J. J.; Stewart, D. R.; Williams, R. S. Electrical Transport and Thermometry of Electroformed Titanium Dioxide Memristive Switches. *J. Appl. Phys.* **2009**, *106*, 124504.
- Adler, S. B.; Chen, X. Y.; Wilson, J. R. Mechanisms and Rate Laws for Oxygen Exchange on Mixed-Conducting Oxide Surfaces. *J. Catal.* **2007**, *245*, 91–109.
- Zhu, H. Y.; Kee, R. J.; Janardhanan, V. M.; Deutschmann, O.; Goodwin, D. G. Modeling Elementary Heterogeneous Chemistry and Electrochemistry in Solid-Oxide Fuel Cells. *J. Electrochem. Soc.* **2005**, *152*, A2427–A2440.
- Gil, Y.; Umrhan, O. M.; Riess, I. Properties of a Solid State Device with Mobile Dopants: Analytic Analysis for the Thin Film Device. *J. Appl. Phys.* **2008**, *104*, 084504.
- Laoire, C. O.; Mukerjee, S.; Abraham, K. M.; Plichta, E. J.; Hendrickson, M. A. Elucidating the Mechanism of Oxygen Reduction for Lithium–Air Battery Applications. *J. Phys. Chem. C* **2009**, *113*, 20127–20134.
- Bishop, S. R.; Duncan, K. L.; Wachsman, E. D. Surface and Bulk Oxygen Nonstoichiometry and Bulk Chemical Expansion in Gadolinium-Doped Cerium Oxide. *Acta Mater.* **2009**, *57*, 3596–3605.
- Adler, S. B. Factors Governing Oxygen Reduction in Solid Oxide Fuel Cell Cathodes. *Chem. Rev.* **2004**, *104*, 4791–4843.
- Kharton, V. V., Ed. *Solid State Electrochemistry I: Fundamentals, Materials and their Applications*; Wiley-VCH: New York, 2009.
- Bard, A. J.; Faulkner, L. R. *Electrochemical Methods*; Wiley: New York, 2008.
- Newman, J.; Thomas-Alyea, K. E. *Electrochemical Systems*, 3rd ed.; Wiley: New York, 2004.
- Weppner, W.; Huggins, R. A. Electrochemical Methods for Determining Kinetic-Properties of Solids. *Annu. Rev. Mater. Sci.* **1978**, *8*, 269–311.
- O'Hayre, R. *Probing Electrochemistry at the Micro Scale: Applications in Fuel Cells, Ionics, and Catalysis*; VDM Verlag: Saarbruecken, Germany, 2008.
- Kalinin, S. V.; Balke, N. Local Electrochemical Functionality in Energy Storage Materials and Devices by Scanning Probe Microscopies: Status and Perspectives. *Adv. Mater.* **2010**, *22*, E193–E209.
- Balke, N.; Jesse, S.; Kim, Y.; Adamczyk, L.; Tselev, A.; Ivanov, I. N.; Dudney, N. J.; Kalinin, S. V. Real Space Mapping of Li-Ion Transport in Amorphous Si Anodes with Nanometer Resolution. *Nano Lett.* **2010**, *10*, 3420–3425.
- Balke, N.; Jesse, S.; Morozovska, A. N.; Eliseev, E.; Chung, D. W.; Kim, Y.; Adamczyk, L.; Garcia, R. E.; Dudney, N.; Kalinin, S. V. Nanometer-Scale Mapping of Ion Diffusion in a Lithium-Ion Battery Cathode. *Nat. Nanotechnol.* **2010**, *5*, 749–754.
- Morozovska, A. N.; Eliseev, E.; Balke, N.; Kalinin, S. V. Local Probing of Ionic Diffusion by Electrochemical Strain Microscopy: Spatial Resolution and Signal Formation Mechanisms. *J. Appl. Phys.* **2010**, *108*, 053712.
- Morozovska, A.; Eliseev, E.; Kalinin, S. V. Electromechanical Probing of Ionic Currents in Energy Storage Materials. *Appl. Phys. Lett.* **2010**, *96*, 222906.
- Dudney, N. J. Solid-State Thin-Film Rechargeable Batteries. *Mater. Sci. Eng., B* **2005**, *116*, 245–249.
- Gruverman, A.; Kholkin, A. Nanoscale Ferroelectrics: Processing, Characterization and Future Trends. *Rep. Prog. Phys.* **2006**, *69*, 2443–2474.
- Kalinin, S. V.; Rodriguez, B. J.; Kim, S. H.; Hong, S. K.; Gruverman, A.; Eliseev, E. A. Imaging Mechanism of Piezoresponse Force Microscopy in Capacitor Structures. *Appl. Phys. Lett.* **2008**, *92*, 152906.
- Christman, J. A.; Woolcott, R. R.; Kingon, A. I.; Nemanich, R. J. Piezoelectric Measurements with Atomic Force Microscopy. *Appl. Phys. Lett.* **1998**, *73*, 3851–3853.

29. Das, S. R.; Williams, D. F.; Webb, J. F. Dependence of the Microstructure of Amorphous-Silicon Thin-Films Prepared by Planar RF Magnetron Sputtering on Deposition Parameters. *J. Appl. Phys.* **1983**, *54*, 3101–3105.
30. Messier, R.; Giri, A. P.; Roy, R. A. Revised Structure Zone Model for Thin-Film Physical Structure. *J. Vac. Sci. Technol., A* **1984**, *2*, 500–503.
31. Messier, R.; Krishnaswamy, S. V.; Gilbert, L. R.; Swab, P. Black a-Si Solar Selective Absorber Surfaces. *J. Appl. Phys.* **1980**, *51*, 1611–1614.
32. Jesse, S.; Kalinin, S. V.; Proksch, R.; Baddorf, A. P.; Rodriguez, B. J. The Band Excitation Method in Scanning Probe Microscopy for Rapid Mapping of Energy Dissipation on the Nanoscale. *Nanotechnology* **2007**, *18*, 435503.
33. Rodriguez, B. J.; Callahan, C.; Kalinin, S. V.; Proksch, R. Dual-Frequency Resonance-Tracking Atomic Force Microscopy. *Nanotechnology* **2007**, *18*, 475504.
34. Kos, A. B.; Hurley, D. C. Nanomechanical Mapping with Resonance Tracking Scanned Probe Microscope. *Meas. Sci. Technol.* **2008**, *19*, 015504. (2008).
35. Polomoff, N. A.; Premnath, R. N.; Bosse, J. L.; Huey, B. D. Ferroelectric Domain Switching Dynamics with Combined 20 nm and 10 ns Resolution. *J. Mater. Sci.* **2009**, *44*, 5189–5196.
36. Zeyen, B.; Virwani, K.; Pittenger, B.; Turner, K. L. Preamplifying Cantilevers for Dynamic Atomic Force Microscopy. *Appl. Phys. Lett.* **2009**, *94*, 103507.
37. Preisach, F. Über die Magnetische Nachwirkung. *Z. Phys.* **1935**, *94*, 277–302.
38. Mayergoyz, I. D. Mathematical-Models of Hysteresis. *Phys. Rev. Lett.* **1986**, *56*, 1518–1521.
39. Ovchinnikov, O.; Jesse, S.; Guo, S.; Seal, K.; Bittachitt, P.; Fujii, I.; Troler-McKinstry, S.; Kalinin, S. V. Local Measurements of Preisach Density in Polycrystalline Ferroelectric Capacitors Using Piezoresponse Force Spectroscopy. *Appl. Phys. Lett.* **2010**, *96*, 112906. (2010).
40. Guo, S.; Ovchinnikov, O.; Curtis, M. E.; Johnson, M. B.; Jesse, S.; Kalinin, S. V. *J. Appl. Phys.* **2010**, *108*, 084103.
41. Jesse, S.; Lee, H. N.; Kalinin, S. V. Quantitative Mapping of Switching Behavior in Piezoresponse Force Microscopy. *Rev. Sci. Instrum.* **2006**, *77*, 073702.
42. Jesse, S.; Kalinin, S. V. Principal Component and Spatial Correlation Analysis of Spectroscopic-Imaging Data in Scanning Probe Microscopy. *Nanotechnology* **2009**, *20*, 085714.
43. Bonnet, N. Some Trends in Microscope Image Processing. *Micron* **2004**, *35*, 635–653.
44. Bosman, M.; Watanabe, M.; Alexander, D. T. L.; Keast, V. J. Mapping Chemical and Bonding Information Using Multivariate Analysis of Electron Energy-Loss Spectrum Images. *Ultramicroscopy* **2006**, *106*, 1024–1032.
45. Jolliffe, I. T. *Principal Component Analysis*; Springer-Verlag: Berlin, Heidelberg, New-York, 2002.
46. Bishop, S. R.; Duncan, K. L.; Wachsman, E. D. Defect Equilibria and Chemical Expansion in Nonstoichiometric Undoped and Gadolinium-Doped Cerium Oxide. *Electrochim. Acta* **2009**, *54*, 1436–1443.
47. Adler, S. B. Chemical Expansivity of Electrochemical Ceramics. *J. Am. Ceram. Soc.* **2001**, *84*, 2117–2119.
48. Zuev, A. Y.; Vylkov, A. I.; Petrov, A. N.; Tsvetkov, D. S. Defect Structure and Defect-Induced Expansion of Undoped Oxygen Deficient Perovskite  $\text{LaCoO}_{3-\delta}$ . *Solid State Ionics* **2008**, *179*, 1876–1879.
49. Lein, H. L.; Wiik, K.; Grande, T. Thermal and Chemical Expansion of Mixed Conducting  $\text{La}_{0.5}\text{Sr}_{0.5}\text{Fe}_{1-x}\text{Co}_x\text{O}_{3-\delta}$  Materials. *Solid State Ionics* **2006**, *177*, 1795–1798.
50. Chen, X.; Yu, J.; Adler, S. B. Thermal and Chemical Expansion of Sr-Doped Lanthanum Cobalt Oxide ( $\text{La}_{1-x}\text{Sr}_x\text{CoO}_{3-\delta}$ ). *Chem. Mater.* **2005**, *17*, 4537–4546.
51. Kharton, V. V.; Kovalevsky, A. V.; Avdeev, M.; Tsipis, E. V.; Patrakeev, M. V.; Yaremchenko, A. A.; Maumovich, E. N.; Frade, J. R. Chemically Induced Expansion of  $\text{La}_2\text{NiO}_{4+\delta}$ -Based Materials. *Chem. Mater.* **2007**, *19*, 2027–2033.
52. Zuev, A. Y.; Tsvetkov, D. S. Oxygen Nonstoichiometry, Defect Structure and Defect-Induced Expansion of Undoped Perovskite  $\text{LaMnO}_{3(\pm)\delta}$ . *Solid State Ionics* **2010**, *181*, 557–563.
53. Rabatic, B. M.; Dimitrijevic, N. M.; Cook, R. E.; Saponjic, Z. V.; Rajh, T. Spatially Confined Corner Defects Induce Chemical Functionality of  $\text{TiO}_2$  Nanorods. *Adv. Mater.* **2006**, *18*, 1033–1037.
54. Kalinin, S. V.; Rodriguez, B. J.; Baddorf, A. P.; Balke, N.; Borisevich, A. Y.; Chang, H. J.; Chen, L. Q.; Choudhury, S.; Jesse, S.; Maksymovych, P. Defect-Mediated Polarization Switching in Ferroelectrics and Related Materials: From Mesoscopic Mechanisms to Atomistic Control. *Adv. Mater.* **2010**, *22*, 314–322.
55. Rodriguez, B. J.; Choudhury, S.; Chu, Y. H.; Bhattacharyya, A.; Jesse, S.; Seal, K.; Baddorf, A. P.; Ramesh, R.; Chen, L. Q.; Kalinin, S. V. Unraveling Deterministic Mesoscopic Polarization Switching Mechanisms: Spatially Resolved Studies of a Tilt Grain Boundary in Bismuth Ferrite. *Adv. Funct. Mater.* **2009**, *19*, 2053–2063.
56. Kalinin, S. V.; Jesse, S.; Rodriguez, B. J.; Chu, Y. H.; Ramesh, R.; Eliseev, E. A.; Morozovska, A. N. Probing the Role of Single Defects on the Thermodynamics of Electric-Field Induced Phase Transitions. *Phys. Rev. Lett.* **2008**, *100*, 155703.